metals

MDPI

Article

Prediction of Surface Wrinkle Defect of Welding Wire Steel ER70S-6 in Hot Bar Rolling Process Using Finite Element Method and Experiments

Qian Liu [1], Yaqiang Tian [1,*], Jinpo Zhai [2], Lu Tian [2], Liansheng Chen [1,*] and Liqing Chen [3,*]

[1] College of Metallurgy and Energy, North China University of Science and Technology, Tangshan 063210, China; liuqian@ncst.edu.cn
[2] Welding Steel Technology Innovation Center of Hebei Province, Technology Center, Tangshan Delong Iron and Steel Co., Ltd., Tangshan 063600, China; lqgzs2005@163.com (J.Z.); haierco@126.com (L.T.)
[3] State Key Laboratory of Rolling and Automation, Northeastern University, Shenyang 110819, China
* Correspondence: tyq@ncst.edu.cn (Y.T.); kyckfk@ncst.edu.cn (L.C.); lqchen@mail.neu.edu.cn (L.C.); Tel.: +86-0315-880-5221 (Liansheng Chen)

Received: 21 October 2020; Accepted: 22 November 2020; Published: 23 November 2020

Abstract: High quality products are demanded due to increasingly fierce market competition. In this paper, the generation of surface wrinkle defect of welding wire steel ER70S-6 was studied by the combination of the experimental method and finite element simulation. Firstly, a thermal compression test was conducted on the Gleeble-3500 thermosimulator under different strain rates and temperatures and a strain dependent Arrhenius-type constitutive function was employed to fit the flow stress–strain curves obtained from the experiments. Then, the elastoplastic constitutive relationship was implemented using radial return mapping algorithm by means of the user subroutine VUMAT of Abaqus/Explicit. A new instability criterion was proposed to predict the possibility of the surface wrinkle defect during the multipass hot bar rolling process. In order to verify the reliability of the finite element model of the six-pass continuous rolling process, the simulated results were compared with experimental data. Finally, the effects of groove width and groove radius on the billet were investigated by the orthogonal test method, and the friction coefficient and rolling temperature. The results show that the groove width and groove radius are key factors to suppress the surface wrinkle defect. Decreasing the groove width can be beneficial for improving the surface quality and reducing the fillet radius. The optimized combination of the rolling process parameters was further applied in an industrial test and the surface quality of the billet was greatly improved.

Keywords: surface wrinkle defect; welding wire steel; orthogonal test method; hot rolling process; finite element method

1. Introduction

With the development of the welding process, the demand for welding wire steel increases year by year. As a common type of welding wire steel, ER70S-6 is a low carbon alloy steel composed of a composite structure of pearlite and ferrite. Due to excellent performance in the drawing and welding process, it is widely used in construction equipment, automotive structures, pressure vessels, pipe fabrication and automatic or semiautomatic welding applications. Welding wire steel is generally produced by the hot bar rolling process, which is one of the most important industrial processes [1–3]. The heated billet is continuously deformed through several pairs of rolls to obtain a certain finished product with smaller cross section dimension and geometry. Due to local instability, surface wrinkle defect easily occurs during rolling process. It is a common surface defect that is hidden under the skin of iron oxide and distributed like a band along the rolling direction, as shown in Figure 1. It may

further develop into a fata quality defect and eventually lead to the failure of the billet during the subsequent manufacturing process [4].

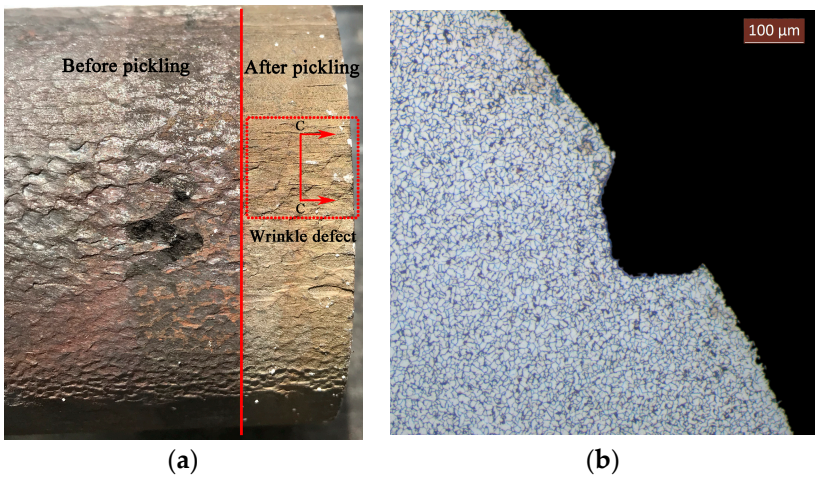

Figure 1. Morphological features of surface wrinkle defect. (**a**) Front view. (**b**) Cross-section view C-C.

Currently, high quality products are demanded due to increasingly fierce market competition [5]. Therefore, in order to minimize or suppress the occurrence of a surface wrinkle defect on materials during the rolling process, many related research works are carried out. In the past, the quality of products mainly depends on the worker's experience [6,7]. The trial and error method not only wastes a lot of time, but also increases the cost. With the rapid development of the computing technology, the finite element method shows great advantages in terms of dealing with large plastic deformation problems. Although the wrinkle defect cannot be found in the finite element software, many certain criteria were developed to predict the occurrence of wrinkle defect, such as the rheological model based on the dislocation theory [8], specific deformation energy [9] and shear fracture model [10]. Then, these criteria are implemented in the finite element model to understand the mechanism of the wrinkle defect. When a certain element satisfies the chosen criterion in the finite element simulation, it is identified as a damage element. The tendency of the surface wrinkle defect in real material can be analyzed according to the number of damage elements in finite element simulation. The effect of roll groove on the surface wrinkle defect was studied using the thermomechanical finite element method, and the temperature change of material in multipass rolling [9–12]. The results show that improving the roll groove and reducing the temperature drop of material are the efficient ways to improve the product quality. Compared to the change of the roll geometry, increasing the initial rolling temperature makes less flow instability. In addition, the deformation characteristic under the hot compression condition was investigated using the Gleeble thermomechanical simulator. The study found that the surface defect was easy to initiate at the position where it is subjected to high stress and large strain at a low temperature range [13,14]. Although many researchers had paid attention to characterize the cause of the surface wrinkle defect and tried to solve the problem, it is not quite well solved because of the complexity of the hot bar rolling process.

The prime objective of this paper is to minimize or suppress the occurrence of the surface wrinkle defect by reducing the deformation instability of the fillet corner of the billet. Since deformation instability is related to the degree of deformation, a new criterion for considering the combined effect of the shear stress, effective stress and effective strain was employed to measure the possibility of surface wrinkle defect occurrence. In this paper, the generation of the surface wrinkle defect was studied by the combination of the experimental method and finite element simulation. The effects of roll geometry, friction coefficient and rolling temperature on the surface wrinkle defect were analyzed utilizing the orthogonal test method. Finally, the combination of rolling process parameters was optimized to improve product quality.

2. Finite Element Model of the Hot Bar Rolling Process

2.1. Constitutive Equations

The material used in the present experiment is welding wire steel ER70S-6. As shown in Table 1, the mass fraction of its main alloying element is given. A thermal compression test was conducted on the Gleeble-3500 thermosimulator (DSI Inc, New York, NY, USA) to obtain the stress–strain relationship of the material. The cylindrical specimens 12 mm in length and 8 mm in diameter were prepared for tests. Figure 2 shows the schematic diagram of the hot compressive deformation experiment. As seen, the specimens were heated to 1200 °C at a rate of 10 °C/s and held for 3 min to homogenize and eliminate thermal gradients. Then, the specimens were cooled down to the deformation temperatures (900, 1000, 1050, 1100, 1150 and 1200 °C) at a rate of 10 °C/s, held for 1 min and compressed with a specified strain rate (0.01, 0.1, 1 and 10 s^{-1}). Finally, the deformed specimen was quenched by water after 60% reduction. The typical true stress–strain curves under different deformation conditions are shown in Figure 3. It is seen that the true stress is strongly affected by deformation temperature and strain rate. As the deformation temperature increases, the deformation resistance decreases. With increasing the strain rate, the deformation resistance increases. The material firstly experiences work hardening, then dynamic recovery and recrystallization occurs.

Table 1. The mass fraction of chemical composition of welding wire steel ER70S-6.

Elements	C	Si	Mn	P	S	Cr	Ni	Cu
wt %	0.068	0.89	1.52	0.012	0.011	0.03	0.01	0.02

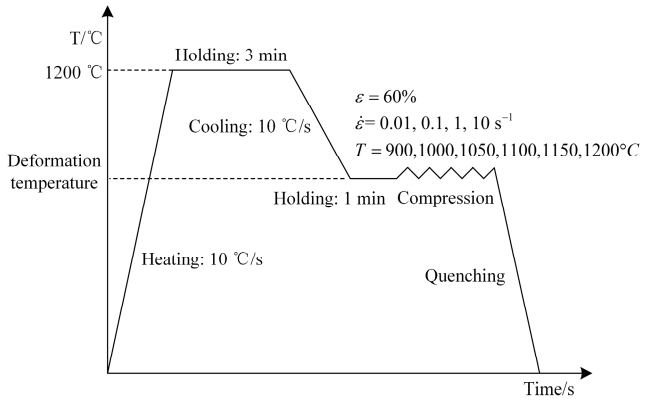

Figure 2. Experiment scheme of hot compressive deformation.

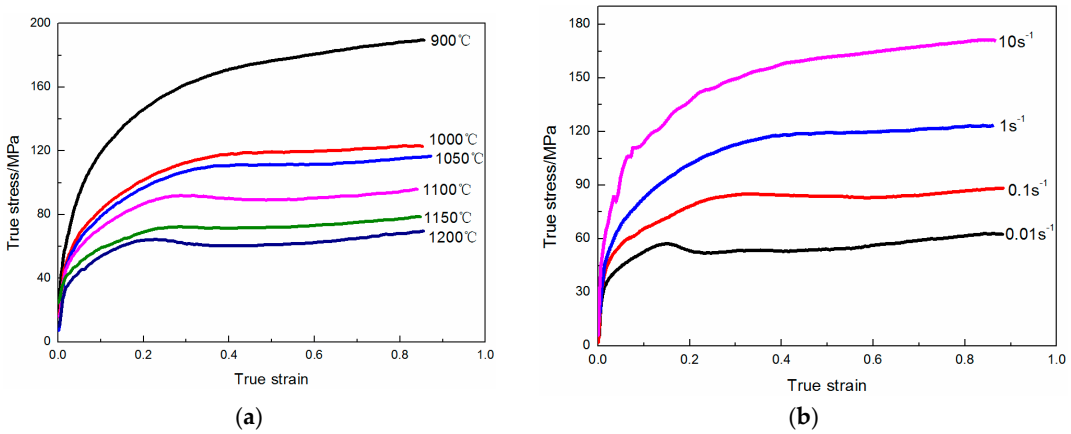

Figure 3. The typical true stress–strain curves under different deformation conditions: (**a**) $\dot{\varepsilon}$ = 1 s^{-1} and (**b**) T = 1000 °C.

The material constitutive relationship over a wide range of temperature can be represented by a strain dependent Arrhenius-type constitutive function, as shown in Equation (1) [15]. The values of Q, A, n and α can be expressed as fifth order polynomial functions of strain in Equation (2). Where, M_1–M_6, N_1–N_6, X_1–X_6 and Y_1–Y_6 are the coefficients of the polynomial; ε is the true stain. Table 2 shows the coefficient of each item in Equation (2). Therefore, the value of flow stress under any deformation temperature and deformation rate can be derived according to Equations (1) and (2).

$$\dot{\overline{\varepsilon}} = A[\sinh(\alpha\overline{\sigma})]^n \exp(-Q/RT) \tag{1}$$

$$\begin{aligned} n &= M_1 + M_2\varepsilon + M_3\varepsilon^2 + M_4\varepsilon^3 + M_5\varepsilon^4 + M_6\varepsilon^5 \\ \alpha &= N_1 + N_2\varepsilon + N_3\varepsilon^2 + N_4\varepsilon^3 + N_5\varepsilon^4 + N_6\varepsilon^5 \\ Q &= X_1 + X_2\varepsilon + X_3\varepsilon^2 + X_4\varepsilon^3 + X_5\varepsilon^4 + X_6\varepsilon^5 \\ \ln A &= Y_1 + Y_2\varepsilon + Y_3\varepsilon^2 + Y_4\varepsilon^3 + Y_5\varepsilon^4 + Y_6\varepsilon^5 \end{aligned} \tag{2}$$

Table 2. Values of material constants of the constitutive equation.

n	α (MPa^{-1})	Q (kJ/mol)	ln$A$ (s^{-1})
M_1 = 8.6719	N_1 = 0.0205	X_1 = 409.4463	Y_1 = 35.2856
M_2 = −32.1982	N_2 = −0.0609	X_2 = −448.1335	Y_2 = −62.8739
M_3 = 92.1619	N_3 = 0.2430	X_3 = 811.1758	Y_3 = 200.3972
M_4 = −118.7672	N_4 = −0.5835	X_4 = −729.4218	Y_4 = −332.5019
M_5 = 69.5087	N_5 = 0.6817	X_5 = 467.9818	Y_5 = 295.7253
M_6 = −13.5810	N_6 = −0.2986	X_6 = −167.2209	Y_6 = −107.3682

According to the Equations (1) and (2), the flow stress can be expressed as an explicit function of the Zener–Hollomon parameter Z. That is:

$$\overline{\sigma} = \frac{1}{\alpha}\ln\left\{\left(\frac{Z}{A}\right)^{\frac{1}{n}} + \left[\left(\frac{Z}{A}\right)^{\frac{2}{n}} + 1\right]^{\frac{1}{2}}\right\} \tag{3}$$

where Z is defined by:

$$Z = \dot{\overline{\varepsilon}}\exp(Q/RT) \tag{4}$$

2.2. Numerical Integration Algorithm of the Strain Dependent Arrhenius-Type Constitutive Equation

The above strain dependent Arrhenius-type equation was implemented in ABAQUS/Explicit with the help of user subroutine VUMAT (6.14, Vélizy-Villacoublay Cedex, France). The methodology adopted here is the radial return mapping algorithm. Firstly, the total incremental strain is assumed to be fully elastic. If the stress state is inside the yield surface at the incremental step, the elastic predictor is true. Otherwise, the plastic corrector procedure is used to ensure the new stress state lies on the yield surface after strain hardening.

Firstly, the total strain tensor can be decomposed into an elastic part and a plastic part:

$$\varepsilon = \varepsilon^{\mathrm{e}} + \varepsilon^{\mathrm{p}} \tag{5}$$

where, the superscript $(\cdot)^{\mathrm{e}}$ and $(\cdot)^{\mathrm{p}}$ refers to the elastic and plastic part.

The stress is calculated according to Hooke's law of elasticity:

$$\sigma = C^{\mathrm{e}} : \varepsilon^{\mathrm{e}} = 2G\varepsilon^{\mathrm{e}} + \lambda\mathrm{trace}(\varepsilon^{\mathrm{e}})I \tag{6}$$

where, C^{e} denotes the fourth-order elasticity tensor.

Therefore, the stress tensor at the time increment $t + \Delta t$:

$$\sigma = C^{\mathrm{e}} : \varepsilon^{\mathrm{e}} = C^{\mathrm{e}} : \left(\varepsilon_t^{\mathrm{e}} + \Delta\varepsilon^{\mathrm{e}}\right) = C^{\mathrm{e}} : \left(\varepsilon_t^{\mathrm{e}} + \Delta\varepsilon - \Delta\varepsilon^{\mathrm{p}}\right) = \sigma^{\mathrm{tr}} - C^{\mathrm{e}} : \Delta\varepsilon^{\mathrm{p}} \tag{7}$$

where, σ and S represent stress and the deviatoric stress, respectively. The superscript $(\cdot)^{\mathrm{tr}}$ refers to the trail test.

$$\sigma^{\mathrm{tr}} = C^{\mathrm{e}} : \left(\varepsilon_t^{\mathrm{e}} + \Delta\varepsilon\right) \tag{8}$$

S^{tr} is defined by:

$$S^{\mathrm{tr}} = \sigma^{tr} + \sigma_m \mathbf{I} \tag{9}$$

$$\sigma_m = -\frac{1}{3}\mathrm{Trace}(\sigma) \tag{10}$$

where σ_m denotes the hydrostatic stress.

$\overline{\sigma}$ is the equivalent stress defined by:

$$\overline{\sigma}^{\mathrm{tr}} = \sqrt{\frac{3}{2} S^{\mathrm{tr}} : S^{\mathrm{tr}}} \tag{11}$$

Therefore,

$$S^{\mathrm{tr}} = \sigma^{tr} - \frac{1}{3}\mathrm{trace}\left(\sigma^{\mathrm{tr}}\right) I \tag{12}$$

Calculate the yield function at the time increment $t + \Delta t$:

$$f = \overline{\sigma}^{\mathrm{tr}} - \sigma_{y0}\left(\overline{\varepsilon}_0^{\mathrm{p}}, \dot{\overline{\varepsilon}}_0^{\mathrm{p}}, T_0\right) \tag{13}$$

where $\overline{\varepsilon}_0^{\mathrm{p}}$, $\dot{\overline{\varepsilon}}_0^{\mathrm{p}}$ and T_0 denotes the effective plastic strain, the effective plastic strain rate and the temperature at the time increment t, respectively.

If the yield function is less than or equal to 0 ($f \leq 0$), the whole increment step is purely elastic. The elastic prediction is true and the local procedure is completed. Then, $S = S^{\mathrm{tr}}$ and the internal state variables will not be updated.

If the yield function is greater than 0 ($f > 0$), the current state is out of the original yield surface. Therefore, the deviatoric stress tensor needs to be recalculated by means of a plastic correction.

$$f = \overline{\sigma} - \sigma_y\left(\overline{\varepsilon}^{\mathrm{p}}, \dot{\overline{\varepsilon}}^{\mathrm{p}}, T\right) = 0 \tag{14}$$

$$\overline{\varepsilon}^{\mathrm{p}} = \overline{\varepsilon}_0^{\mathrm{p}} + \Delta\overline{\varepsilon}^{\mathrm{p}} \tag{15}$$

$$\dot{\overline{\varepsilon}}^{\mathrm{p}} = \frac{\Delta\overline{\varepsilon}^{\mathrm{p}}}{\Delta t} \tag{16}$$

$$\Delta\overline{\varepsilon}^{\mathrm{p}} = \sqrt{\frac{2}{3}\Delta\varepsilon^{\mathrm{p}} : \Delta\varepsilon^{\mathrm{p}}} \tag{17}$$

$$\overline{\sigma} = \sqrt{\frac{3}{2} S : S} \tag{18}$$

$$S = S^{\mathrm{tr}} - \sqrt{6} G \Delta\overline{\varepsilon}^{\mathrm{p}} n \tag{19}$$

where, n is the unit normal direction of the yield surface. According to the associative flow rule, it is defined by:

$$n = \frac{S^{\mathrm{tr}}}{\sqrt{S^{\mathrm{tr}} : S^{\mathrm{tr}}}} \tag{20}$$

For the fully coupled thermal–mechanical problem, temperature is considered as the nonnegligible parameter. Therefore, the change in the temperature of the billet should be calculated accurately. It can be define by the change of internal energy U:

$$\Delta T = \frac{U}{\rho c_p} \tag{21}$$

where, ρ denotes the material density and c_p denotes the specific heat capacity.

According to the thermal energy equilibrium, the change of internal energy has to be equal to the summation of the heat transfer and heat generation due to the plastic deformation.

$$U = \eta\sigma : \Delta\varepsilon^{\mathrm{p}} - \frac{\partial}{\partial x} \cdot q \tag{22}$$

where, η denotes the inelastic heat fraction and q denotes heat flux.

Therefore,

$$T = T_0 + \Delta T \tag{23}$$

Finally, the yield function can be written as a function of $\Delta\overline{\varepsilon}^{\mathrm{p}}$. The Newton–Raphson method is adopted to solve the non-linear equation.

$$\Delta\overline{\varepsilon}^{\mathrm{p}}_{i+1} = \Delta\overline{\varepsilon}^{\mathrm{p}}_{i} - \frac{f(\Delta\overline{\varepsilon}^{\mathrm{p}})}{f'(\Delta\overline{\varepsilon}^{\mathrm{p}})} \tag{24}$$

$$\left|\Delta\overline{\varepsilon}^{\mathrm{p}}_{i+1} - \Delta\overline{\varepsilon}^{\mathrm{p}}_{i}\right| \le \Delta\overline{\varepsilon}^{\mathrm{p}}_{tol} \tag{25}$$

where $\Delta\overline{\varepsilon}^{\mathrm{p}}_{tol}$ is the user-defined error tolerance (10×10^{-6}). When Equation (25) is satisfied, the Newton–Raphson iteration method is completed.

2.3. Finite Element Modeling

Hot bar rolling process is a fully coupled thermal–mechanical problem [7,16]. In order to investigate the surface wrinkle defect, three dimensional finite element model of the six-pass continuous rolling process was established in Abaqus/Explicit, as shown in Figure 4. The square billet with cross-section 160 mm × 160 mm was used. According to the symmetry of the billet and the boundary conditions, only one quarter of the rolling configuration was established to reduce the run time. The x, y and z axis in the model was coincident with the reduction, transversal and rolling direction, respectively. The billet was assumed as the elastoplastic deformable body and the rolls were defined as the analytical rigid bodies. The Young's modulus E is an elastic parameter, which generally decreases with increasing deformation temperature. The material behavior obeyed the isotropic work hardening model, the von Mises yield criterion and the Prandtl–Reuss flow rule [17]. An 8 node thermo-mechanical coupled brick element C3D8RT was used and the total billet was meshed into 59,312 elements. It just refined the elements near the billet fillet corner margin where the severe deformation happened. In addition, the arbitrary Lagrangian–Eulerian method was applied in simulation to improve mesh quality of the deformation zone and eliminate the occurrence of mesh distortion [18,19]. At the beginning of rolling simulation, an initial speed 0.8 m/s was applied to the billet. An angular velocity was applied in the center reference point of the roll, which was consistent with the actual production, as shown in Table 3. The contact type between the billet and roll was defined as "surface to surface contact". The Coulomb friction model was used for the contact and the friction factor was set as 0.3 [20]. The billet was rolled with initial temperature of 1120 °C. The roll and ambient temperature were 200 °C and 20 °C, respectively. The heat transfer conditions include the heart transfer between the billet and rolls, as well as the convection and radiation of the free surface of billet with the environment. The contact heat transfer coefficient between the billet and rolls was set as 15 kW/(m^2·°C) based on actual conditions. The heat transfer condition of the convection and radiation between the free surface of billet and

ambience was set as 20 W/(m^2·°C). The conversion factor of heat dissipated by plastic deformation work was set as 0.9.

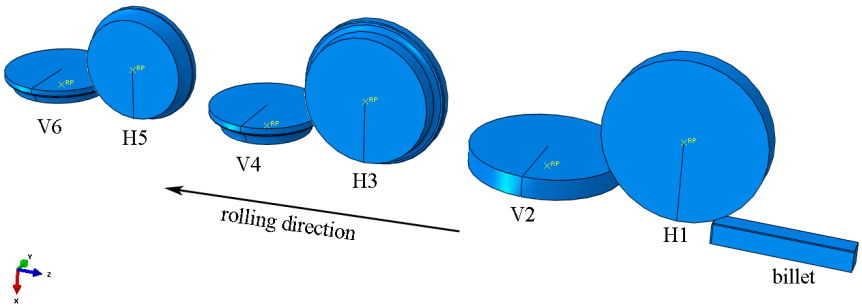

Figure 4. Finite element model of six passes the rough rolling process.

Table 3. Technological parameters for the rough rolling process.

Pass	Groove	Roll Diameter/mm	Elongation Coefficient	Angular Velocity/rad·s^{-1}
H1	flat	600	1.233	0.415
V2	flat	600	1.231	0.526
H3	oval	600	1.439	0.678
V4	round	480	1.310	1.188
H5	oval	480	1.406	1.531
V6	round	480	1.304	2.117

2.4. Experimental Verification

Figure 5 shows that the simulated and experimental billet geometry at the exit of the third pass. In Figure 5a,c, the billet geometry at the exit of the third pass was obtained by the manual rubbing method in the experiment. It should be noted that the sample is located in the center of the billet. Figure 5b,d was obtained using the exterior edges type of visible edges in Abaqus post-processing. As can be seen from Figure 5, there was a slight difference between the simulated and experimental billet geometry.

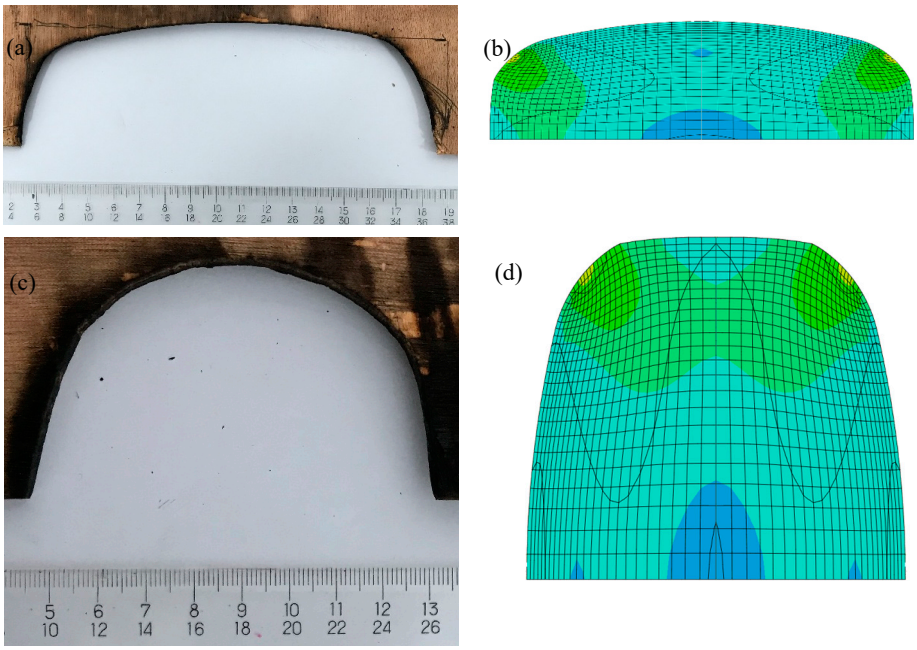

Figure 5. Comparison of experimental and simulated billet geometry at the exit of the third pass:

(**a**) The top surface of the experimental billet geometry. (**b**) The top surface of the simulated billet geometry. (**c**) The lateral surface of the experimental billet geometry. (**d**) The lateral surface of the simulated billet geometry.

In Figure 6, billet dimensions at the exit of each pass of the continuous rolling process between experimental and finite element simulation results were compared to validate the effectiveness of the proposed finite element model [8,21]. The results show that the simulated results are in good agreement with the experimental values. After six passes the continuous rolling process, the experimental height and width of rolled round bar were 78 mm and 76 mm, respectively. In simulations, the height and width of that were 77.1 mm and 74.6 mm, respectively. Therefore, the relative errors were 1.15% and 3.16%, respectively.

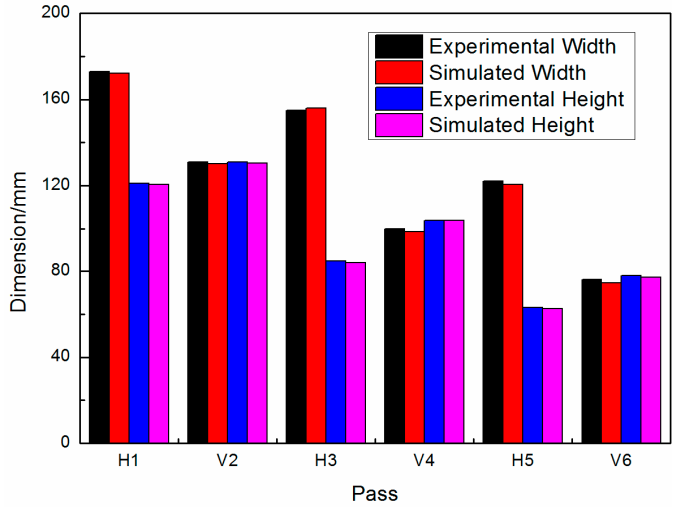

Figure 6. Comparison of experimental and simulated billet sizes at exit of each pass.

3. Results and Discussion

3.1. Analysis of Hot Bar Rolling Deformation

As shown in Figure 7, the effective plastic strain, effective stress and temperature distribution of billet at the exit of the third pass of rough rolling were instigated with the finite element simulations. Compared to other areas, the maximum of equivalent von Mises stress and the total equivalent plastic strain of the fillet corner were greater. However, the surface temperature of billet was much lower than the center area. In Figure 8, point A and B were chosen to investigate the temperature change, which were located at the center and fillet edge of the billet respectively. Before rolling, the temperature of Point B dropped slowly due to air convection. When the roll contacted with the billet, it dropped rapidly because the roll temperature was lower than the billet during the rolling deformation. After rolling, the surface temperature gradually recovered due to heat transfer from center area to the surface. However, the temperature of Point A rose due to heat generation of plastic deformation and then slightly reduced because of heat conduction [22]. Therefore, the characteristics of the stress, strain and temperature distribution show that the fillet corner of the billet was more susceptible to surface defects in the hot bar rolling process.

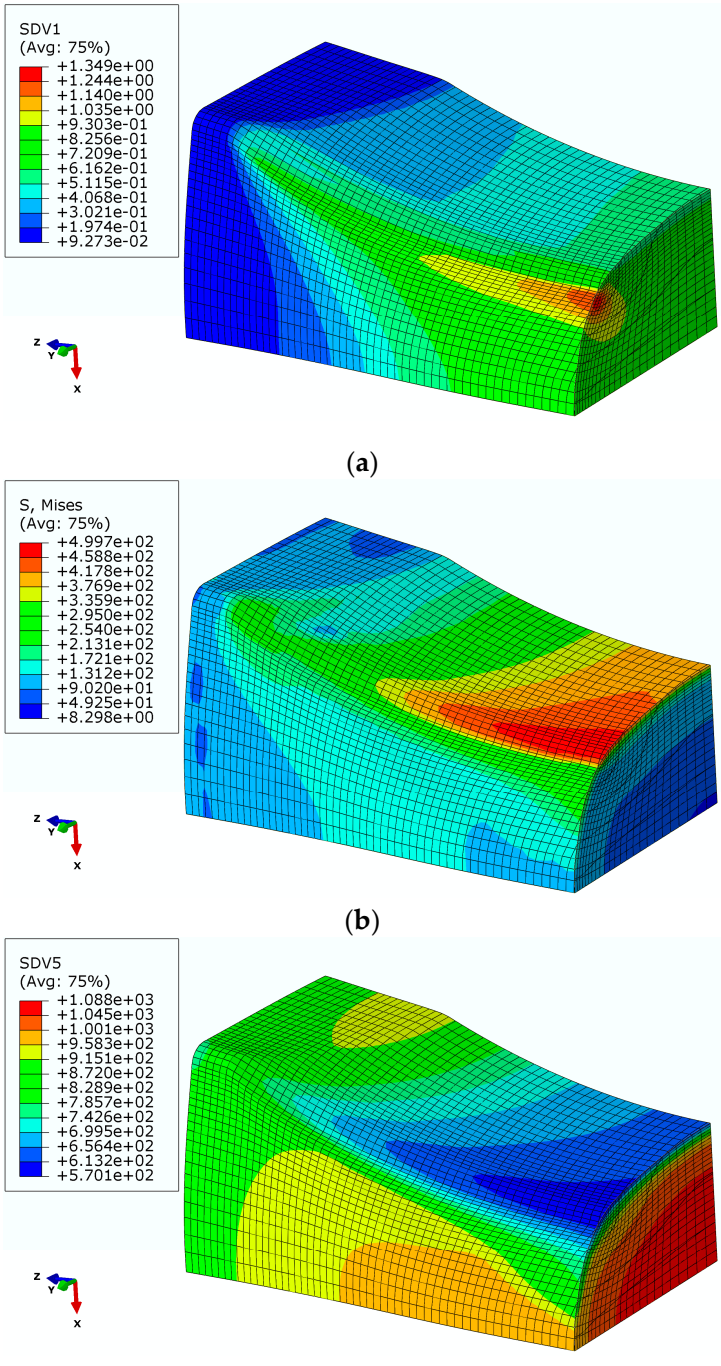

Figure 7. FEM analysis result of the third pass of the roughing mill. (**a**) Effective plastic strain. (**b**) Effective stress (MPa) and (**c**) temperature (°C).

3.2. A New Criterion for Predicting Surface Wrinkle Defect

For the material forming process, the ductile fracture criterion was often used to predict the initiation and propagation of microcracks, which can be expressed as an integral function of the stress and plastic strain tensor. Unlike the experiments, the surface wrinkle defect cannot be directly observed in the finite element simulation. Comprehensively considering the effects of shear stress, equivalent

stress and equivalent plastic strain on the surface wrinkle defect, a new criterion for predicting the surface wrinkle defect is proposed:

$$\int_0^{\overline{\varepsilon}} \frac{\tau_{xy}}{\overline{\sigma}} d\overline{\varepsilon} = C \tag{26}$$

where τ_{xy}, $\overline{\sigma}$ and $\overline{\varepsilon}$ denotes the shear stress, effective stress and effective plastic strain, respectively; C denotes the critical value, which represents the maximum value of Equation (26) when the surface wrinkle defect does not generate. The initial pass sequence of rough rolling in the hot bar rolling process was set to six passes: box–box–oval–circle–oval–circle. In order to reduce the frequency of the roll change and enhance production efficiency, 150 mm × 150 mm square billet was replaced with 160 mm × 160 mm. Meanwhile, two flat rolls were used instead of box grooves (Figure 9). However, the surface wrinkle defect had occurred on the billet surface after the rough rolling process. Therefore, the original hot bar rolling process was simulated and investigated using the finite element method. The integral value of all elements was calculated from the post-processing and the maximum value 0.2 was taken as the critical value for predicting the occurrence of the surface wrinkle defect. During the finite element simulation analysis, the surface defect is supposed to occur at any element where the integral value reaches the critical value.

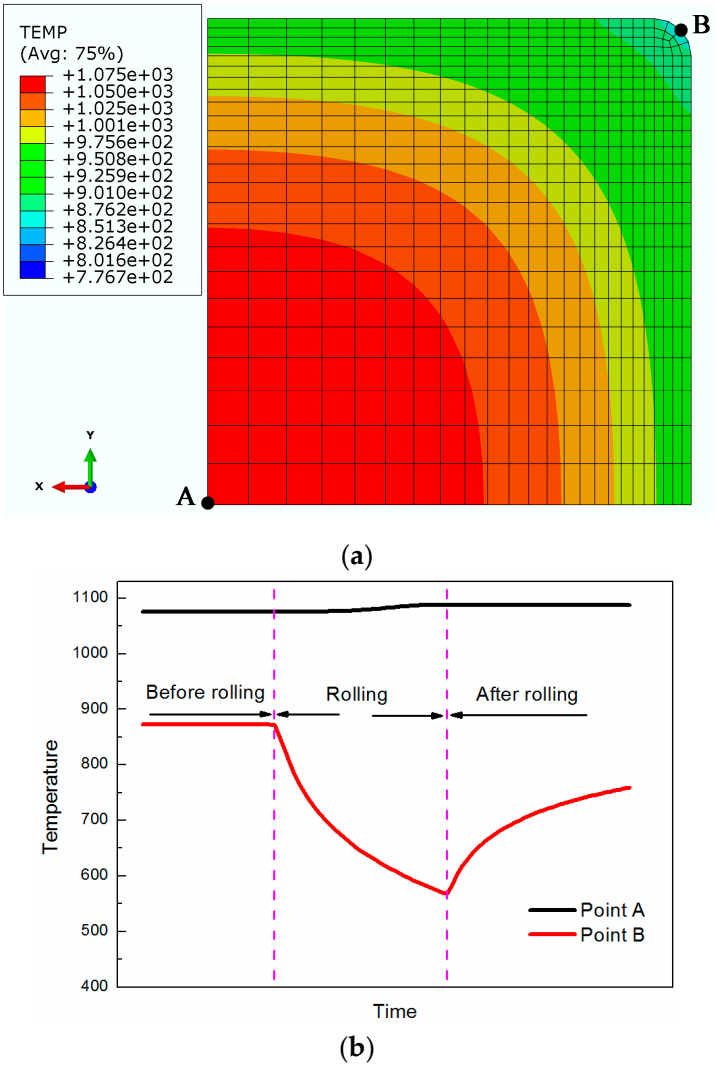

Figure 8. Temperature change at different position of the billet. (**a**) The location of the chosen point A and B. (**b**) Temperature history in the corner and edge of the billet.

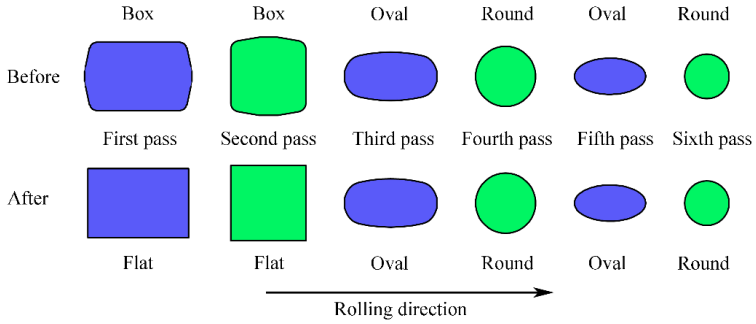

Figure 9. Comparison of previously and newly designed six-pass rolling sequence.

3.3. Determination of Surface Wrinkle Defect Location and Its Evolution

Figure 10 shows the distribution of damage elements of the billet after passing through the oval hole (the 3rd pass). It can be seen that the damage elements were concentrated at the lateral side of the fillet corner. The billet was subjected to compressive deformation in the height direction during the rolling process [23]. It extended in the longitudinal direction and spread in the width direction. Compared to other locations, the fillet corner of the billet had not only greater deformation, but also lower temperature. This special deformation condition caused larger deformation gradient and the instability phenomenon. Due to the greatly different movement speed, the irregular surface quality, which is called the wrinkle defect, occurred [4,24].

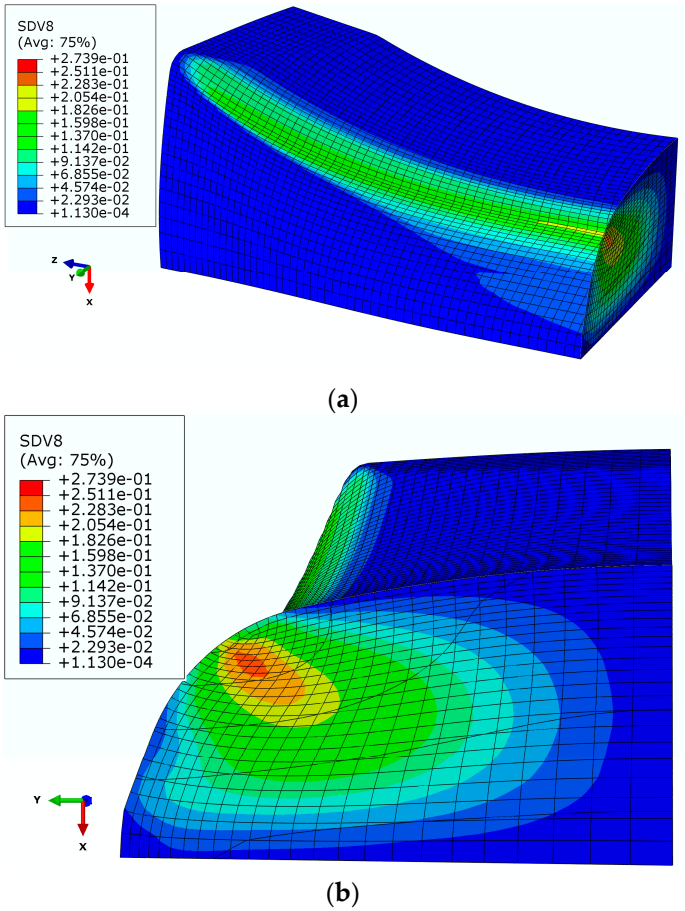

Figure 10. The damage elements of the billet after passing through the oval hole (the 3rd pass). (**a**) The main view. (**b**) The front view.

Figure 11 shows the variation trend of the integral value of a damage element along with the rolling progress. When the billet enters the roll, the damage value of the element at the fillet corner firstly increased rapidly and then slowly. It indicates that surface wrinkle defect easily occurred in the early stage of rolling process.

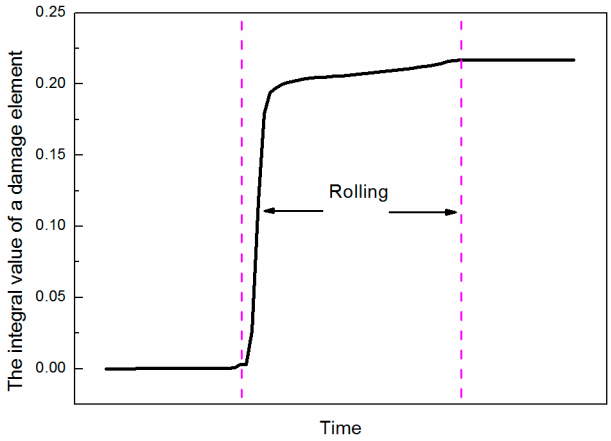

Figure 11. Variation of the integral value of a damage element along with the rolling progress.

3.4. Effect of Rolling Process Parameters on the Surface Wrinkle Defect

The degree of the surface wrinkle defect was affected by process parameters, such as groove size, friction coefficient and rolling temperature. The parameters of groove size play a significant role in the deformation behavior of the billet, especially groove radius and groove width in Figure 12 [2,25,26]. In order to evaluate the role of the parameters on surface wrinkle defect, the orthogonal test method was introduced. The orthogonal test method is a kind of designing method to study the multifactor optimization scheme [27,28]. It has the advantages of saving time and reducing costs. The values of the process parameters were chosen in Table 4. The selected orthogonal table of L_9 (3^4), including four factors and three levels, was adopted to arrange nine cases. The nine finite element models were established in Abaqus/Explicit according to the nine groups of process parameters. The number of the damage elements in the finite element simulation is presented in Table 5.

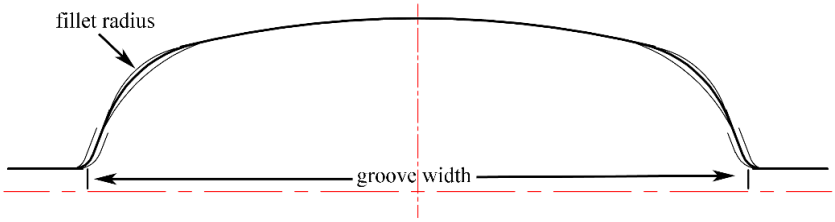

Figure 12. Roll groove parameters: fillet radius and groove width.

Table 4. Influencing factors of the surface wrinkle defect for an orthogonal analysis.

Factors / Levels	Groove Radius/mm	Groove Width/mm	Friction Coefficient	Rolling Temperature/°C
Level 1	25	160	0.26	1090
Level 2	30	162	0.28	1120
Level 3	35	164	0.3	1150

Table 5. The simulation results using the orthogonal test method.

Case	Groove Radius/mm	Groove Width/mm	Friction Coefficient	Rolling Temperature/°C	The Number of the Damage Elements
1	25	160	0.26	1090	1962
2	25	162	0.28	1120	2350
3	25	164	0.3	1150	2769
4	30	160	0.28	1150	2615
5	30	162	0.3	1090	2996
6	30	164	0.26	1120	3327
7	35	160	0.3	1120	3692
8	35	162	0.26	1150	4030
9	35	164	0.28	1090	3831

Table 6 presents the influences of the four process parameters on the number of damage elements. R denotes the significance level of the factors, and K1 to K3 represent the sum of the numbers of the damage elements corresponding to level 1 to 3. According to the orthogonal test theory, the factor with a larger R is more significantly influential than other factors. Similarly, the level with a larger k is superior to other levels. Hence, the order of the influences on the surface wrinkle defect was groove radius > groove width > friction coefficient > rolling temperature. The optimal combination for the best surface quality was groove radius (level 1)–groove width (level 1)–friction coefficient (level 2)–rolling temperature (level 1).

Table 6. Analysis of the simulation results using the range method.

Parameters	Groove Radius/mm	Groove Width/mm	Friction Coefficient	Rolling Temperature/°C
K1	7081	8269	9319	8789
K2	8938	9376	8796	9369
K3	11,553	9927	9457	9414
k1	2360.33	2756.33	3106.33	2929.67
k2	2979.33	3125.33	2932	3123
k3	3851	3309	3152.33	3138
R	1490.67	552.67	220.33	208.33
Order	groove radius > groove width > friction coefficient > rolling temperature			
Optimal combination	groove radius1-groove width1-friction coefficient2-rolling temperature1			

In Figure 13, variations of the number of damage elements for different process parameters are presented. R, W, F and T represent groove radius, groove width, friction coefficient and rolling temperature, respectively. The numbers 1, 2 and 3 represent levels 1, 2 and 3, respectively. It shows that the groove radius and groove width had strong effects on the number of damage elements. For example, as the groove radius increased, the number of damage elements rose. The friction coefficient had an optimized range between 0.26 and 0.3. When the rolling temperature increased, the number of damage elements increased. That is probably because the fillet corner dissipated quickly despite raising the roll temperature.

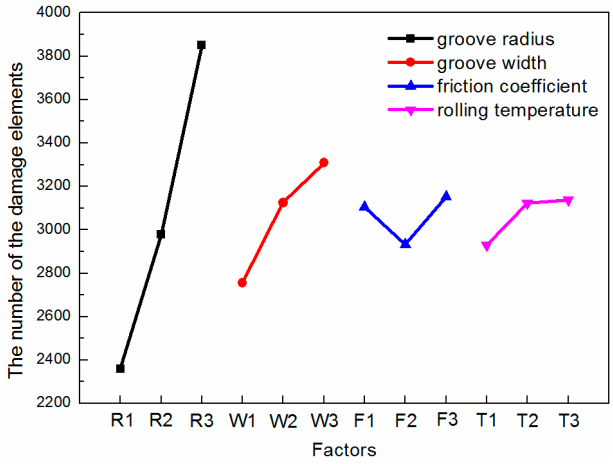

Figure 13. Profiles of the number of the damage elements for different process parameters.

3.5. Industrial Testing Verification

Figure 14 shows the morphology of the surface wrinkle defect located at different positions and its distribution. The black area in Figure 14e represents the distribution of the surface wrinkle defect on the cross section of the billet. It can be seen that the distribution of the surface wrinkle defect corresponds to the four fillets of the billet. The experimental results agreed well with the above finite element simulation.

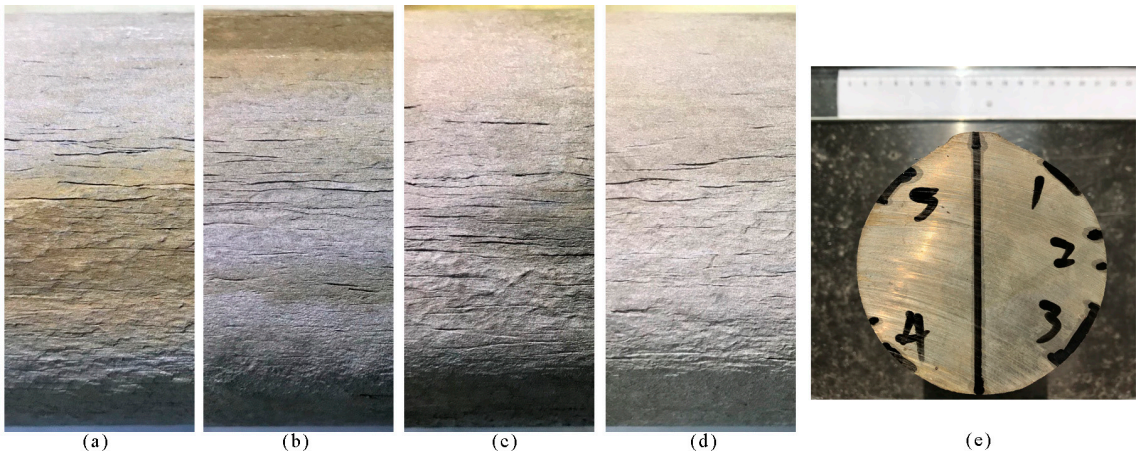

Figure 14. The morphology of surface wrinkle defects located at different positions and its distribution. (**a**–**d**) represent the morphology of surface wrinkle defects located at area 1, 3, 4 and 5, respectively. (**e**) The distribution of surface wrinkle defects in the cross section of the billet.

In order to verify the above analysis, the industrial testing was conducted where the optimized combination of the rolling process parameters was adopted (groove radius: 25 mm; groove width: 160 mm; friction coefficient: 0.28 and rolling temperature: 1090 °C). The surface wrinkle defects before and after optimization of process parameters are shown in Figure 15. The depth of the wrinkle defect was measured along the circumference of the billet after six passes the continuous rolling process. Then these values were sorted in descending order and the largest ten values were chosen for comparison. Figure 16 shows the depth measurement of surface wrinkle defects before and after optimization of process parameters. When the optimized combination of the rolling process parameters was adopted, the maximum depth of wrinkle defect decreased from 291.4 to 150.1 μm, and the average depth of wrinkle defect decreased from 155.2 to 79.6 μm. Therefore, the surface quality of the billet in the rough rolling process was greatly improved after optimization.

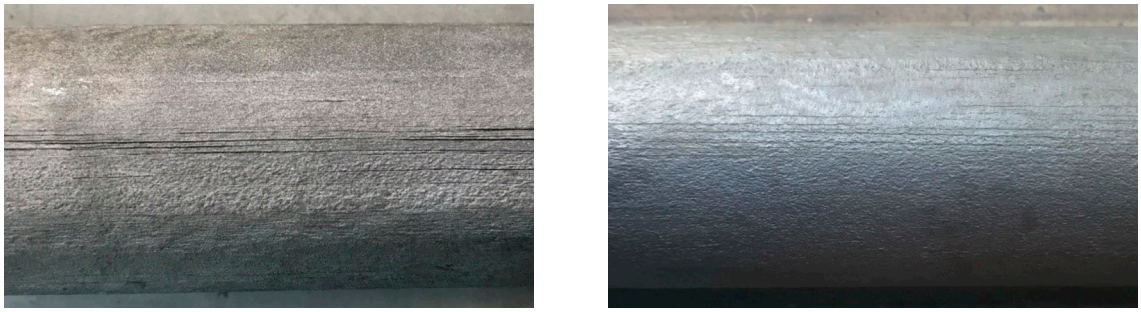

(**a**) (**b**)

Figure 15. The comparison of surface wrinkle defects before and after optimization of process parameters. (**a**) Before optimization of process parameters. (**b**) After optimization of process parameters.

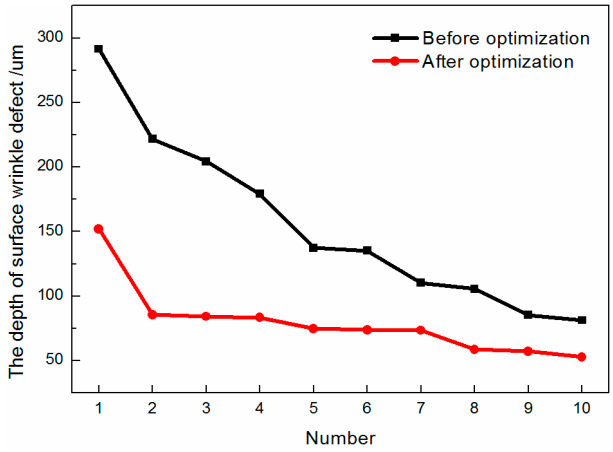

Figure 16. The depth measurement of surface wrinkle defects before and after optimization of process parameters.

4. Conclusions

In the present work, the surface wrinkle defect of welding wire steel ER70S-6 in hot bar rolling process was investigated based on the finite element method and experiments. The following conclusions are drawn.

(1) The deformation behavior of welding wire steel ER70S-6 under different deformation conditions was obtained by hot compression tests. The true stress decreased with the increase of deformation temperature when the strain rate was fixed. The true stress increased with the increase of strain rate when the deformation temperature was fixed. A strain dependent Arrhenius-type constitutive function was determined by fitting the flow stress–strain curves.

(2) The thermal–mechanical finite element modeling of the six-pass continuous rolling process was established in Abaqus/Explicit. Based on radial return mapping algorithm, the elastoplastic constitutive model was implemented with the help of user subroutine VUMAT. The simulation results agreed well with the experiments in terms of billet dimensions at the exit of each pass of the continuous rolling process.

(3) The combination effects of different process parameters on the surface wrinkle defect were investigated through the orthogonal test, including groove size, friction coefficient and rolling temperature. The impact sequence of the process parameters for the surface wrinkle defect was groove radius > groove width > friction coefficient > rolling temperature. The industrial testing result agreed well with the simulation. The change of groove size was an effective way to suppress surface wrinkle defect, especially decreasing the groove radius and the groove width.

Author Contributions: Conceptualization, Q.L. and L.C. (Liansheng Chen); Methodology, Q.L. and Y.T.; validation, J.Z. and L.T.; investigation, Q.L., J.Z. and L.T.; writing—original draft preparation, Q.L. and Y.T.; writing—review and editing, L.C. (Liansheng Chen) and L.C. (Liqing Chen). All authors have read and agreed to the published version of the manuscript.

Funding: This research was supported by the National Science Foundation of Hebei Province of China (Grant No. E2018209278, E2017209121), Department of Education of Hebei Province (Grant No. QN2019051, ZD 2019064, ZD2018242), National Science Foundation of China (Grant No. 51474091), and Liaoning Provincial Natural Science Foundation of China (Grant No. 2019-KF-25-01).

Conflicts of Interest: The authors declare no conflict of interest.

References

1. Spuzic, S.; Narayanan, R.; Kovacic, Z.; Arachchige, D.H.; Abhary, K. Roll pass design optimisation. *Int. J. Adv. Manuf. Technol.* **2017**, *91*, 999–1005. [CrossRef]
2. Oduguwa, V.; Roy, R. A review of rolling system design optimisation. *Int. J. Mach. Tool. Manuf.* **2006**, *46*, 912–928. [CrossRef]
3. Hanoglu, U.; Šarler, B. Hot Rolling Simulation System for Steel Based on Advanced Meshless Solution. *Metals* **2019**, *9*, 788. [CrossRef]
4. Son, I.H.; Lee, J.D.; Choi, S.; Lee, D.L.; Im, Y.T. Deformation behavior of the surface defects of low carbon steel in wire rod rolling. *J. Mater. Process. Technol.* **2008**, *201*, 91–96. [CrossRef]
5. Agarwal, K.; Shivpuri, R. On line prediction of surface defects in hot bar rolling based on Bayesian hierarchical modeling. *J. Intell. Manuf.* **2015**, *26*, 785–800. [CrossRef]
6. Shinokura, T.; Takai, K. A new method for calculating spread in rod rolling. *J. Appl. Metalwork.* **1982**, *2*, 94–99. [CrossRef]
7. Kim, S.Y.; Im, Y.T. Three-dimensional finite element analysis of non-isothermal shape rolling. *J. Mater. Process. Technol.* **2002**, *127*, 57–63. [CrossRef]
8. Milenin, A.A.; Dyja, H.; Mróz, S. Simulation of metal forming during multi-pass rolling of shape bars. *J. Mater. Process. Technol.* **2004**, *153*, 108–114. [CrossRef]
9. Kwon, H.C.; Lee, H.W.; Kim, H.Y.; Im, Y.T.; Park, H.D.; Lee, D.L. Surface wrinkle defect of carbon steel in the hot bar rolling process. *J. Mater. Process. Technol.* **2009**, *209*, 4476–4483. [CrossRef]
10. Na, D.H.; Lee, Y. A study to predict the creation of surface defects on material and suppress them in caliber rolling process. *Int. J. Precis. Eng. Manuf.* **2013**, *14*, 1727–1734. [CrossRef]
11. Kawano, M.; Isogawa, S.; Kawanishi, K. Evaluation of roll pass designs by thermal mechanical FEM simulation. *Electr. Furn. Steel* **1999**, *70*, 255–260.
12. Awais, M.; Lee, H.W.; Im, Y.T.; Kwon, H.C.; Byon, S.M.; Park, H.D. Plastic work approach for surface defect prediction in the hot bar rolling process. *J. Mater. Process. Technol.* **2008**, *201*, 73–78. [CrossRef]
13. Zhang, J.; Kwon, H.C.; Kim, H.Y.; Byon, S.M.; Park, H.D.; Im, Y.T. Micro-cracking of low carbon steel in hot-forming processes. *J. Mater. Process. Technol.* **2005**, *162*, 447–453. [CrossRef]
14. Lee, H.W.; Kwon, H.C.; Awais, M.; Im, Y.T. Instability map based on specific plastic work criterion for hot deformation. *J. Mech. Sci. Technol.* **2007**, *21*, 1534–1540. [CrossRef]
15. Samantaray, D.; Mandal, S.; Bhaduri, A.K. A comparative study on Johnson Cook, modified Zerilli-Armstrong and Arrhenius-type constitutive models to predict elevated temperature flow behaviour in modified 9Cr–1Mo steel. *Comp. Mater. Sci.* **2009**, *47*, 568–576. [CrossRef]
16. Kang, S.H.; Im, Y.T. Three-dimensional thermo-elastic–plastic finite element modeling of quenching process of plain-carbon steel in couple with phase transformation. *Int. J. Mech. Sci.* **2007**, *49*, 423–439. [CrossRef]
17. Miehe, C. On the representation of Prandtl-Reuss tensors within the framework of multiplicative elastoplasticity. *Int. J. Plast.* **1994**, *10*, 609–621. [CrossRef]
18. Liu, Q.; Han, J.T.; Tian, Y.Q.; Zheng, X.P.; Song, J.Y.; Chen, L.S. Analysis of sheared edge quality in rotary blanking process based on Lemaitre damage model. *Chinese J. Eng.* **2017**, *39*, 1198–1206.
19. Ertürk, S.; Brocks, W.; Bohlen, J.; Letzig, D.; Steglich, D. A constitutive law for the thermo-mechanical modelling of magnesium alloy extrusion. *Int. J. Mater. Form.* **2012**, *5*, 325–339. [CrossRef]
20. Qin, Q.; Zhang, D.T.; Zang, Y.; Guan, B. A simulation study on the multi-pass rolling bond of 316L/Q345R stainless clad plate. *Adv. Mech. Eng.* **2015**, *7*, 1687814015594313. [CrossRef]

21. Byon, S.M.; Na, D.H.; Lee, Y. Effect of roll gap adjustment on exit cross sectional shape in groove rolling—Experimental and FE analysis. *J. Mater. Process. Technol.* **2009**, *209*, 4465–4470. [CrossRef]
22. Said, A.; Lenard, J.G.; Ragab, A.R.; Elkhier, M.A. The temperature, roll force and roll torque during hot bar rolling. *J. Mater. Process. Technol.* **1999**, *88*, 147–153. [CrossRef]
23. Lee, Y. *Rod and Bar Rolling: Theory and Applications*; CRC Press: New York, NY, USA, 2004; pp. 9–28.
24. Filipović, M.; Eriksson, C.; Överstam, H. Behaviour of surface defects in wire rod rolling. *Steel Res. Int.* **2006**, *77*, 439–444. [CrossRef]
25. Nordén, K.; Jonsson, S. A study of surface deformation during wire-rod rolling of high speed steels using experimental and computational techniques. *Steel Res. Int.* **2007**, *78*, 876–883. [CrossRef]
26. Topno, R.; Gupta, D.S.; Singh, U.P.; Roy, B.; Jha, S. Improvement in the surface quality of ball bearing steel rounds at Bar Mill. *Scand. J. Metal.* **2002**, *31*, 20–24. [CrossRef]
27. Xia, S.; Lin, R.; Cui, X.; Shan, J. The application of orthogonal test method in the parameters optimization of PEMFC under steady working condition. *Int. J. Hydrogen Energy* **2016**, *41*, 11380–11390. [CrossRef]
28. Zhang, Z.; Fang, H.; Yan, H.; Jiang, Z.; Zheng, J.; Gan, Z. Influencing factors of GaN growth uniformity through orthogonal test analysis. *Appl. Therm. Eng.* **2015**, *91*, 53–61. [CrossRef]